J. Fluid Mech. (2002), *vol.* 462, *pp.* 341–363. © 2002 Cambridge University Press
DOI: 10.1017/S0022112002008376 Printed in the United Kingdom

Life of a flapping liquid sheet

By E. VILLERMAUX AND C. CLANET

Institut de Recherche sur les Phénomènes Hors Equilibre, Université de Provence, Aix-Marseille I–CNRS, Technopôle de Château-Gombert, 49, rue Frédéric Joliot-Curie, 13384 Marseille Cedex 13, France

(Received 19 September 2000 and in revised form 14 January 2002)

A round liquid jet with density ρ, surface tension σ and diameter D_0 impacting a solid circular surface at normal incidence with velocity U_0 takes the form of a radially expanding sheet whose thickness decreases with distance from the impact point. When the sheet develops in a still environment with density $\rho_a = \alpha\rho$, it destabilizes, provided the impacting Weber number $We = \rho U_0^2 D_0/\sigma$ is larger than about $40\alpha^{-1/2}$, as a result of a shear instability with the surrounding medium, in a sinuous, flag-like motion. We show how the instability properties set both the radial extent of the liquid sheet and the drop formation process at its rim. The shear instability gives the liquid a flag-like motion, ultimately triggering a Rayleigh–Taylor instability at the rim of the sheet which disintegrates, at the radial location R, into disjointed droplets of size d such that

$$R/D_0 \sim \alpha^{-2/3} We^{-1/3} \quad \text{and} \quad d/D_0 \sim \alpha^{-2/3} We^{-1}.$$

The features of the sheet instability, its radius and the droplet sizes are determined experimentally for a broad range of control parameters, using different liquids and ambient-medium densities.

1. Introduction

Most natural or man-made atomization processes involve, at least transitorily, the formation of a liquid sheet before the formation of drops from an initially compact volume of liquid. There are numerous examples of specific applications using sprays for which the quality of the droplet dispersion has a direct impact on performance, reliability or comfort, ranging from agricultural sewage through liquid and diesel propulsion, to sprayed cosmetics (Bayvel & Orzechowski 1993; Lefebvre 1989). In these contexts, the need to have an *a priori* estimation of the typical droplet size and, better, of the whole droplet size distribution in terms of the external control parameters is frequently expressed. In this respect, knowledge of the transition from sheet to drops is of practical interest.

The inspiration of Félix Savart was of a more heuristic nature when he devised a simple process to form an axisymmetric liquid sheet by letting a round liquid jet impact a flat circular surface (Savart 1833). An account of the contribution of this seminal work, collected in four consecutive papers, to subsequent developments is given in Clanet & Villermaux (2002).

In the contributions inspired by Savart, particularly the experimental ones (see e.g. Taylor 1959*a*, *b* and Huang 1970) various aspects of the problem have been studied regarding the shape and the radial extension of the sheet, and its stability, but a systematic study of the droplet formation from the sheet as it breaks has never

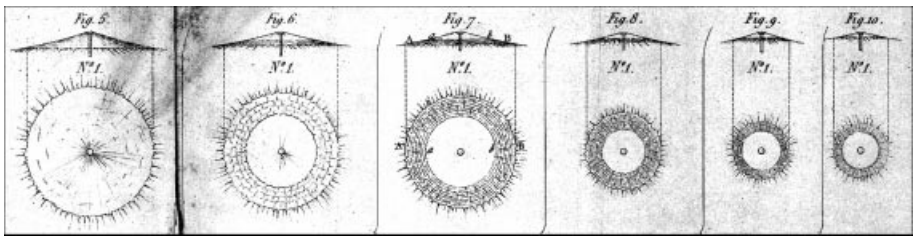

FIGURE 1. Top and side views of an axisymmetric liquid sheet resulting from the impact of a round liquid jet on a flat disc, in the regime analysed in this paper, as first depicted by Félix Savart in 1833. The jet impact velocity is kept constant equal to $10\,\mathrm{m\,s^{-1}}$ and its diameter decreases gradually from left to right by an overall ratio of 6 between Fig. 5 ($D_0 = 14.4\,\mathrm{mm}$) and Fig. 10 ($D_0 = 2.4\,\mathrm{mm}$). The overall shape of the sheet is insensitive to gravity in this limit. Savart also notes that the sheet diameter decreases with increasing velocity for a given jet diameter. (Extract from Plate 4 of Savart 1833).

been attempted. Taylor (1959*b*) merely notes that "The drops are on the average of order 1 to 3 mm diameter so that they were of order 100 times the thickness of the sheet (i.e. from which they detach)" and later in the same paper "So far no mechanism has been put forward to describe the separation of the fluid contained in these edges from the continuous part of the sheet." This is curious since the breaking of the sheet into disjointed droplets is an obvious feature of the problem, and understanding the size of the droplets detaching from the sheet is *a priori* a question of equal interest to the question of understanding its radial extension from the impact location to the breaking region. Complete studies on the drop formation process from liquid sheets are scarce due less to the lack of interest in the physics of divided matter in the nineteenth century than to the lack of reliable experimental tools to measure droplets and characterize their distribution (the observations of Savart were made by eye . . . !). As Lord Rayleigh speculated in 'applications of photography' (Rayleigh 1891) present digital and high-speed video capabilities allow progress on this issue.

Clanet & Villermaux (2002) have investigated the smooth regime of the liquid sheet development, a regime in which the sheet development is basically independent of the medium in which it develops and in which the global features of the sheet (its radial extension) and detailed features (the size of the drops detaching from it) are intrinsic to the physical properties of the liquid. In the present paper, which concerns higher impact Weber numbers, the surrounding medium will be shown to play a dynamical role in both the sheet diameter, and the droplet size. We will show that these two quantities are linked to each other and that understanding the processes by which the droplets form provides *de facto* the sheet extension.

The distinct properties of this new regime are presented in § 2. Interacting with the ambient medium, the sheet destabilizes in a flapping motion and, in contrast to the trend for the smooth regime, the sheet diameter decreases with increasing impact velocity. This had been identified by Savart (figure 1). In § 3, we discuss the nature of the interaction and we analyse quantitatively the features of the instability involved in this problem in § 4. Then § 5 is devoted to the analysis of a destabilization criterion of the sheet rim, the sheet diameter and droplet sizes, before the possible extension of the results to other related configurations is discussed in the concluding § 6.

2. Flag regime: sheet diameter and droplet size

2.1. *Experimental set-up and methods*

The set-up is identical to the one used in Marmottant, Villermaux & Clanet (2000) and Clanet & Villermaux (2002) to which the reader is referred for details. A round liquid jet impacts a flat solid circular surface with velocity U_0 and forms a liquid sheet that expands radially. The results presented here have been obtained with a potential, non-turbulent liquid jet (of water $\rho = 1000\,\mathrm{kg\,m^{-3}}$, $\sigma = 72 \times 10^{-3}\,\mathrm{N\,m^{-1}}$, or ethanol $\rho = 800\,\mathrm{kg\,m^{-3}}$, $\sigma = 24 \times 10^{-3}\,\mathrm{N\,m^{-1}}$) of diameter $D_0 = 2.7\,\mathrm{mm}$ or 3 mm, impacting on a solid surface of diameter $D_i = 6\,\mathrm{mm}$, in ambient air ($\rho_a = 1.2\,\mathrm{kg\,m^{-3}}$). It was possible to immerse the jet and the impacting device in a large tank open at its top, which could be filled with a dense gas, SF_6, whose density at atmospheric pressure is $\rho_a = 6\,\mathrm{kg\,m^{-3}}$.

A thin argon-ion laser (1 W at 488 nm) sheet making the liquid, seeded with a fluorescent dye, visible as a corrugated ribbon could be fitted perpendicular to the liquid surface, allowing the study of the spatial development of its instability. The droplet distributions were obtained from backward illuminated video images digitized using a Neotech 8 bit A/D converter and an appropriate thresholding technique. Time-resolved sequences of the sheet dynamics were obtained with a Kodak 4500HS high-speed video camera.

2.2. *Sheet diameter and droplet size*

The radial development of the liquid sheet from the jet impact location is accompanied in this regime by a distinct flapping motion which gives the sheet a 'blurred and stirred' visual aspect, in the words of Savart. As shown on figure 2, this undulatory motion is characterized by a regular spacing λ between the crests (see also Huang 1970). The wavelength of this undulation is a decreasing function of the jet velocity U_0. For U_0 about $10\,\mathrm{m\,s^{-1}}$, λ is of the order of a centimetre. The frequency of the disturbances at the sheet rim is of the order of 1 kHz, consistent with the distinct flapping tone audible in this regime. Also shown on figure 2(*b*) is a side view of the sheet highlighting the azimuthal corrugations of the wave crests. The spacing between these corrugations is not easily quantifiable and is roughly, although no precise measurements are available, proportional to the primary wavelength λ.

Once this flapping motion appears, the sheet radius starts to decrease as the Weber number is further increased. This happens for a smaller Weber number when the density of the surrounding environment is higher, as shown on figure 3: the phenomenon occurs for $We \gtrsim 10^3$ with the water/air combination, and for $We \gtrsim 500$ with the water/SF_6 combination. The rate of decrease is slower than was the rate of increase of the sheet radius in the smooth regime (see Clanet & Villermaux 2002 who have also compiled measurements from other authors), and follows a trend which is apparently independent of the ambient density, though the absolute magnitude depends on ρ_a (figure 3).

As figure 2 suggests, the liquid sheet disintegrates at a substantially smaller scale than the primary wavelength λ, via indentations of the rim from which small droplets detach. The droplet size (figure 4) is smaller and also decays much faster with increasing jet velocity U_0 (or with increasing Weber number $We = \rho U_0^2 D_0/\sigma$, as will be shown later) than in the previously analysed smooth regime. These are the distinct, and salient features of the 'flag regime' that we wish to investigate in the rest of the paper. We begin with the study of the basic flapping motion, whose origin is discussed in the next section.

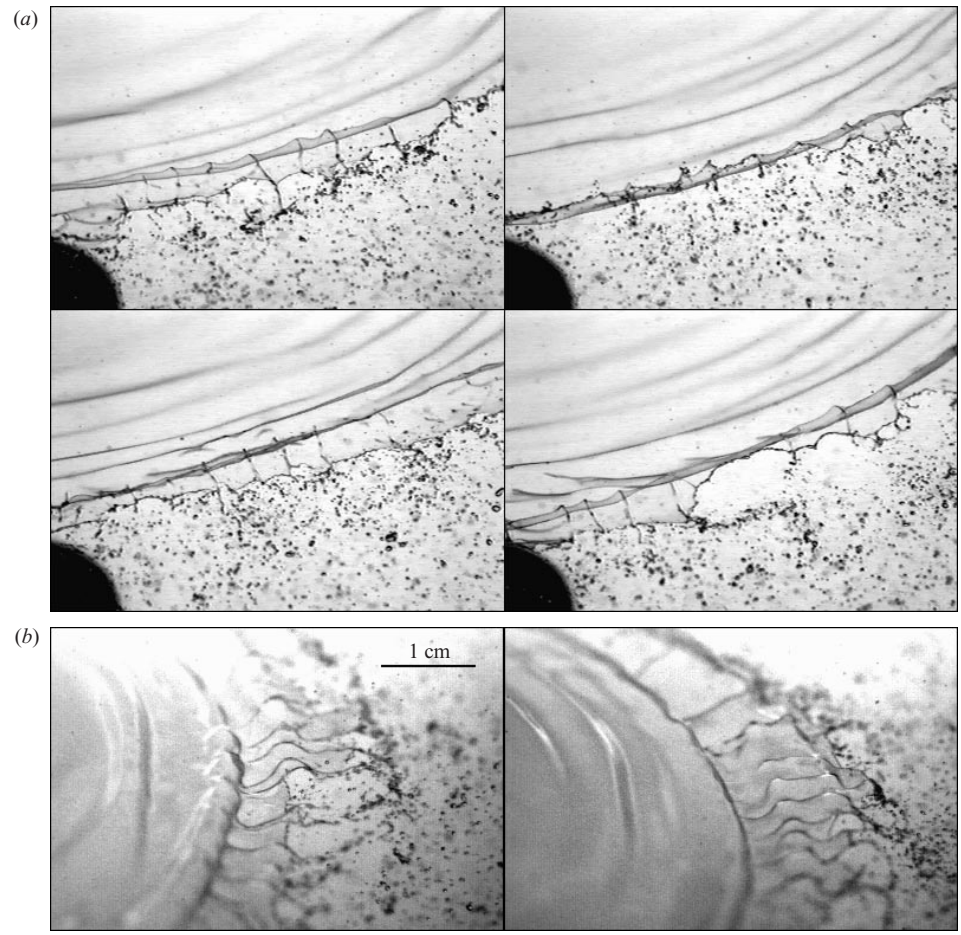

FIGURE 2. (*a*) Snapshots of the destabilization of the moving sheet due to the shear instability in still ambient air. (*b*) Side view highlighting the azimuthal corrugations of the wave crests.

3. Mode selection and wavelength

3.1. *Instability mechanism*

The undulatory shape of the sheet as it propagates at constant velocity in a still environment results from a Kelvin–Helmholtz type of instability, as first analysed, in the context of liquid sheets, by Squire (1953), York, Stubbs & Tek (1953) and Hagerty & Shea (1955). The relevant mechanism explaining the instability was provided by Rayleigh (1879) (see also Lamb 1932 for historical references). The coupling of the sheet disturbances on both sides by the pressure inside the liquid allows only two destabilization modes: an antisymmetrical, sinuous mode, and a symmetrical, dilatational mode (see figure 5).

We first provide a qualitative argument similar to the one derived by Villermaux (1998) for shear instabilities between parallel, infinite media explaining why the sinuous mode is the preferred unstable mode. Then we discuss the condition for the instability to occur and the wavelength at which it is most amplified. By momentum conservation, the velocity in the liquid sheet is conserved and equal to its value just downstream of the impartor's lip. In the following we neglect the weak momentum

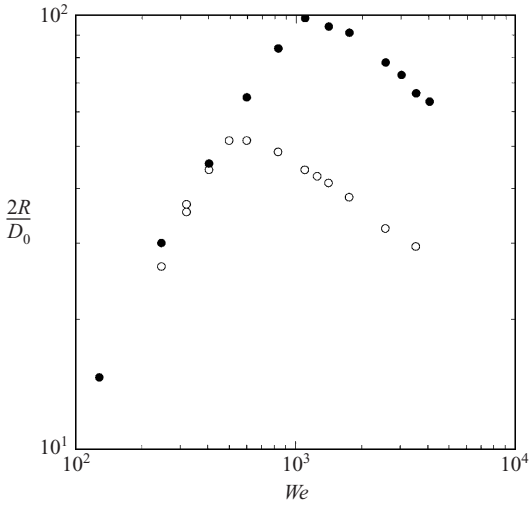

FIGURE 3. Diameter of the flat liquid sheet $2R$ normalized by the jet diameter D_0 versus the impact Weber number $We = \rho U_0^2 D_0/\sigma$ (the liquid is water, $\rho = 1000\,\mathrm{kg\,m^{-3}}$). The two sets of measurements are obtained with two different ambient gas densities: •, air ($\rho_a = 1.2\,\mathrm{kg\,m^{-3}}$); ○, SF_6 ($\rho_a = 6\,\mathrm{kg\,m^{-3}}$).

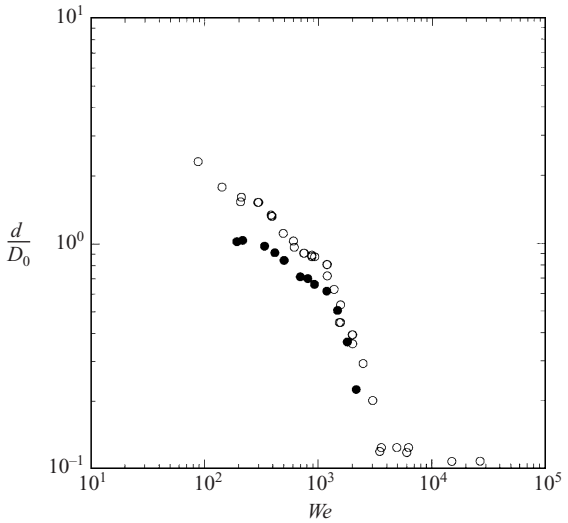

FIGURE 4. Droplet mean arithmetic diameter d/D_0 versus Weber number. There is a strong inflection around $We = 10^3$ (the ambient medium is air, $\rho_a = 1.2\,\mathrm{kg\,m^{-3}}$). •, Ethanol ($\rho = 800\,\mathrm{kg\,m^{-3}}$); ○, water ($\rho = 1000\,\mathrm{kg\,m^{-3}}$). $D_0 = 2.7\,\mathrm{mm}$.

loss at the impact (see Clanet & Villermaux 2002 for a discussion of this effect), and use the jet velocity U_0 as the velocity of the liquid in the sheet.

Let us first consider the sinuous mode (figure 5*a*). Let λ be the wavelength of the undulation, with an amplitude ξ. We choose λ larger than the sheet thickness h *a priori*. Because of incompressibility, the pressure difference in the surrounding medium in the vicinity of the sheet between the crests of the liquid sheet and the

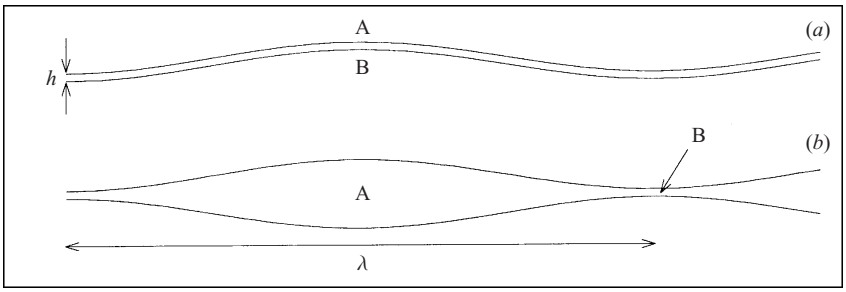

FIGURE 5. Sketch of the two possible destabilization modes of a liquid sheet moving in a still ambient medium: (*a*) sinuous mode, (*b*) dilatation mode.

troughs is given by

$$\delta p = p_B - p_A \sim \rho_a U_0^2 \frac{\xi}{\lambda}. \tag{1}$$

The growth rate of the instability $r_S = \dot{\xi}/\xi$ derives from a balance of force per unit length in the direction perpendicular to the sheet:

$$\ddot{\xi} \sim r_S^2 \xi \sim \frac{1}{\rho}\frac{\delta p}{h}, \tag{2a}$$

that is

$$r_S \sim \frac{U_0}{\lambda}\sqrt{\frac{\rho_a}{\rho}}\sqrt{\frac{\lambda}{h}}. \tag{2b}$$

Note that $r_S h/U_0 \sim (h/\lambda)^{1/2}$, that is $r_S h/U_0 \sim (kh)^{1/2}$ with $k = 2\pi/\lambda$ the undulation wavenumber.

Consider now the dilatational mode (figure 5*b*). The pressure difference δp given in (1) now sustains a flow from the pinched regions of the sheet, corresponding to the troughs of the undulation in the surrounding phase, towards the adjacent thickened regions of the sheet, which correspond to the crests. Since the crests and the troughs are separated by a distance $\lambda/2$, the velocity u of this inviscid induced flow in the liquid in the direction parallel to the sheet is such that

$$\dot{u} \sim \frac{1}{\rho}\frac{\delta p}{\lambda}, \tag{3}$$

and mass conservation is such that

$$hu \sim \lambda\dot{\xi}, \quad \text{i.e.} \quad \dot{u} \sim \frac{\lambda}{h}\ddot{\xi} = \frac{\lambda}{h} r_D^2 \xi. \tag{4}$$

Therefore, the growth rate of the dilatational mode of instability r_D is

$$r_D \sim \frac{U_0}{\lambda}\sqrt{\frac{\rho_a}{\rho}}\sqrt{\frac{h}{\lambda}}. \tag{5}$$

Note that $r_D h/U_0 \sim (kh)^{3/2}$ and that r_D differs from the growth rate of the sinuous mode r_S by a factor $kh \sim h/\lambda$. This factor is, in practice, always much smaller than unity. The reason is that the wavelength selected by this instability, λ, for which the destabilizing pressure $\rho_a U_0^2$ and the curvature restoration constraint σ/λ due to

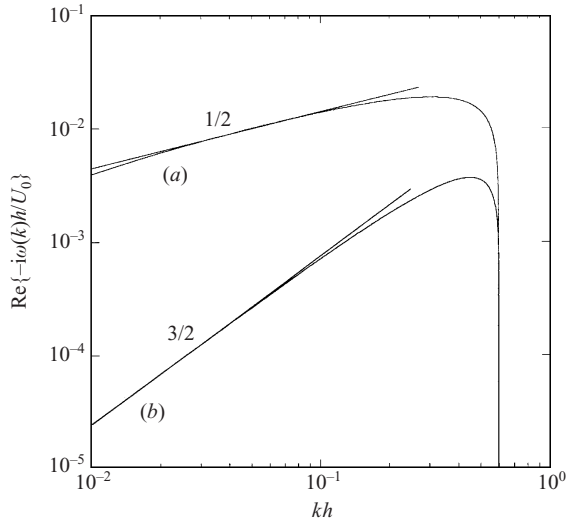

FIGURE 6. Dispersion relations of the two destabilization modes: (*a*) sinuous mode, (*b*) dilatation mode. $We_h = 500$, $\alpha = 1.2 \times 10^{-3}$.

capillarity are balanced is such that

$$\lambda \sim \frac{\sigma}{\rho_a U_0^2}, \tag{6}$$

and this makes the factor h/λ of order $(\rho U_0^2 h/\sigma)(\rho_a/\rho)$. When the sheet-thickness-based Weber number $We_h = \rho U_0^2 h/\sigma$ is of the order of 100, and when the liquid sheet moves in a much less dense environment such as a gas phase, as in many situations and as in the present study in particular, the sinuous unstable mode is thus preferred.

Taking interface disturbances proportional to $\mathrm{e}^{\mathrm{i}kx-\mathrm{i}\omega t}$, where x is the sheet propagation direction, and with $\kappa = kh$, $\Omega = \omega h/U_0$ and $\alpha = \rho_a/\rho$, the dispersion relations of this instability can be written

$$(\Omega - \kappa)^2 \, \Psi\left(\frac{\kappa}{2}\right) + \alpha\Omega^2 = \frac{\kappa^3}{We_h}, \tag{7}$$

with $\Psi(\frac{1}{2}\kappa) = \tanh(\frac{1}{2}\kappa)$ for the sinuous mode and $\Psi(\frac{1}{2}\kappa) = 1/\tanh(\frac{1}{2}\kappa)$ for the dilatational mode. These dispersion relations are displayed on figure 6 for $We_h = 500$ and $\alpha = 1.2 \times 10^{-3}$ (a typical water–air experiment) to illustrate their consistency with the above trends. Note that, as anticipated, the sinuous mode amplifies wavelengths much larger than the sheet thickness, so that $\Psi(\frac{1}{2}\kappa) \approx \frac{1}{2}\kappa$ in practice.

3.2. *Threshold*

Unlike the shear Kelvin–Helmholtz instability between two infinite media (in the absence of gravity perpendicular to the interface) which occurs even for vanishingly small shear, the destabilization of a sheet of finite thickness presents a threshold below which the sheet is stable for all wavenumbers. Indeed, as can be seen from equation (7), and also equation (10) below, the sheet-thickness-based Weber number $We_h = \rho U_0^2 h/\sigma$ must be larger than 2 for a range of wavenumbers to be unstable. In this Weber number and owing to the instability mechanism described in § 3.1, the velocity U_0 stands for the velocity difference between the phases, whatever the frame of reference, i.e. the temporal instability problem is Galilean invariant. The

reason for this distinction lies in the peculiar form of the group velocity dependence of the capillary waves at small k in the two cases. Let us consider α as very small for simplicity. The dispersion relation of the capillary waves on the interface at rest is $\omega^2 = \sigma k^3/\rho$ for an infinite extension of the liquid in the direction perpendicular to the interface, and is $\omega^2 = \sigma k^3/(\rho \tanh(\frac{1}{2}kh))$ for a liquid layer of thickness h, giving in the long-wavelength limit $kh \ll 1$, $\omega^2 = 2\sigma k^2/\rho h$. The group velocity in both cases is thus $v_g = \frac{3}{2}\sqrt{\sigma k/\rho}$ for the infinite medium, and $v_g = \sqrt{2\sigma/\rho h}$ for the finite size layer.

In the infinite liquid thickness limit, the group velocity of the waves decreases continuously as k goes to zero since, because of incompressibility, the inertia of the liquid is proportional to the wavelength $2\pi/k$. There will thus, in this limit, always exist a wavenumber range for which the group velocity is smaller than a given velocity difference U_0 with the less dense phase, which sets the destabilizing pressure scale discussed in § 3.1, i.e. $\rho_a U_0^2$. As soon as there is a velocity difference between the phases, the instability occurs.

Now, the group velocity of the waves on a sheet with a finite thickness has a non-zero minimum value as k goes to zero, equal to $\sqrt{2\sigma/\rho h}$, precisely because the inertia of the liquid is fixed by the sheet thickness, independently of the wavelength. The velocity difference with the less dense phase U_0 thus must be larger than $\sqrt{2\sigma/\rho h}$ for an instability to be possible. Otherwise, the capillary waves propagate without amplification as can be seen from equation (7) (see also Taylor 1959*a*). This condition implies

$$U_0 > \sqrt{\frac{2\sigma}{\rho h}}, \quad \text{i.e.} \quad We_h > 2, \tag{8}$$

as can be seen, again, from equations (7) and (10), providing the threshold condition.

Note that the dynamics of these liquid sheets in the long-wave limit bears a strong similarity with fluid–structure interaction problems, as first investigated by Bourrières (1939). The generic problem is the buckling of a pipe conveying fluid (see the review by Païdoussis & Li 1993). Leaving aside the flexural rigidity of the pipe which has no counterpart in Newtonian liquids, the two problems are analogues, the mass per unit length of the pipe m playing the role of the density ρ_a of the outer medium and the axial tension of the pipe T the role of the liquid surface tension σ, as can be seen from the evolution equation of the lateral deflection of the pipe envelope $y(x,t)$

$$(m + \rho S)\frac{\partial^2 y}{\partial t^2} + (\rho S U_0^2 - T)\frac{\partial^2 y}{\partial x^2} + 2\rho S U_0 \frac{\partial^2 y}{\partial x \partial t} = 0,$$

where ρS denotes the mass per unit length of the liquid in the pipe. The dispersion relation of the above equation is equivalent to the long-wave limit of equation (7) (see also De Langre & Ouvrard 1999).

4. Mode selection on a continuously thinning sheet

4.1. *Dispersion relation*

The thickness $h(r)$ of a radially expanding liquid sheet resulting from the impact of a jet on a solid axisymmetric surface decreases with the radial distance r. It has been shown in Clanet & Villermaux (2002) that, as a consequence of mass and momentum conservation, the thinning of the sheet is described by

$$h(r) = \frac{D_0^2}{8r} \tag{9}$$

until a particular effect at the rim of the sheet fixes its radius R. In the smooth regime, the value of R is fixed by the equality of the incoming, conserved momentum flux ρU_0^2 with the capillary constraint at the rim $2\sigma/h(R)$. When the sheet sustains a sinuous, flag-like instability, it will be shown in § 5 that the mechanism which causes the sheet to disperse into droplets, and therefore which limits the radius of the continuous part of the sheet is specific and directly associated with the features of the flag instability.

The thinning of the sheet along the radius r does not alter the selection of the order of magnitude of the instability mode since, as discussed above, the most amplified wavelength (6) is independent of the sheet thickness. The associated growth rate is, in turn, a function of the thickness: when $We_h \gg 2$, the instability is increasingly amplified as the sheet thins, as can be seen from equation (2*b*) and figure 6, and its growth is slowed down as We_h approaches 2. If it is expected that the most amplified wavelength at any radial position r on the sheet will scale like equation (6), its precise value depends on the relative history of each mode in the dispersion relation (7) incorporating its sensitivity to the local sheet thickness (9) accounted for by the thickness-based Weber number. The dispersion relation $\Omega(\kappa)$ of the sinuous mode is, according to (7) in the limit $\kappa \ll 1$,

$$\left(1+\frac{2\alpha}{\kappa}\right)\Omega = \kappa\left\{1 \pm \sqrt{\frac{2\alpha}{\kappa}\left(\frac{2}{We_h}-1\right)+\frac{2}{We_h}}\right\}, \tag{10}$$

providing, when Ω is split into a real part Ω_r and an imaginary part Ω_i,

$$\Omega_r = \frac{\kappa}{1+2\alpha/\kappa}, \tag{11}$$

$$\Omega_i = \frac{(2\kappa)^{1/2}}{1+2\alpha/\kappa}\left\{\alpha\left(1-\frac{2}{We_h}\right)-\frac{\kappa}{We_h}\right\}^{1/2} \tag{12}$$

where only the positive determination of Ω_i in the unstable range has been retained. Weihs (1978) provides a similar result in axisymmetric coordinates.

Defining the dimensionless radius and wavenumber as $\tilde{r} \equiv 16r/D_0$ and $\tilde{k} \equiv kD_0$, we rewrite (11) and (12) accounting for the radial evolution of the thickness (9) as

$$\frac{\omega_r D_0}{U_0} = \frac{\tilde{k}}{1+\alpha\tilde{r}/\tilde{k}} \tag{13}$$

$$\frac{\omega_i D_0}{U_0} = \frac{(\alpha\tilde{k}\tilde{r})^{1/2}}{1+\alpha\tilde{r}/\tilde{k}}\left\{1-\frac{\tilde{r}}{We}-\frac{\tilde{k}}{\alpha We}\right\}^{1/2}, \tag{14}$$

where $We = \rho U_0^2 D_0/\sigma$. The amplification factor at the radial position r of an initial disturbance of amplitude $a(k,0)$ is such that

$$s(\tilde{k},\tilde{r}) = \ln\left(\frac{a(\tilde{k},\tilde{r})}{a(\tilde{k},0)}\right) = \int_0^t \omega_i \,\mathrm{d}t,$$

that is,

$$s(\tilde{k},\tilde{r}) = \int_0^{\tilde{r}} \omega_i \frac{\mathrm{d}r}{v_g}$$

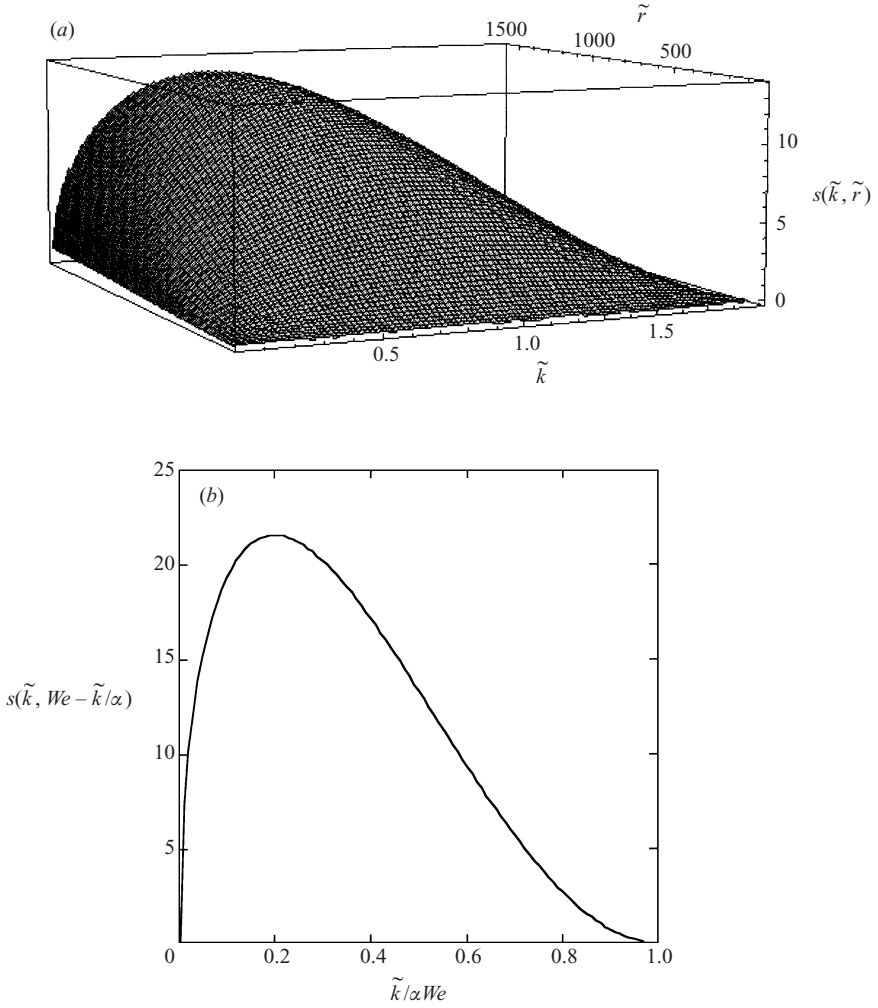

FIGURE 7. (*a*) Amplification factor $s(\tilde{k},\tilde{r})$ of equation (15). (*b*) Maximal amplification given by equation (16). $We = 1600, \alpha = 1.2/1000$.

with $v_g = \mathrm{d}\omega_r/\mathrm{d}k$ the group velocity of a modulation of wavenumber k at the radial location r. From equations (13) and (14), we have

$$s(\tilde{k},\tilde{r}) = \frac{1}{16}\int_0^{\tilde{r}} \mathrm{d}r \frac{1+\alpha r/\tilde{k}}{1+2\alpha r/\tilde{k}} (\alpha \tilde{k} r)^{1/2} \left\{1 - \frac{r}{We} - \frac{\tilde{k}}{\alpha We}\right\}^{1/2}. \tag{15}$$

4.2. *Most amplified wavenumber and spatial growth*

The shape of the amplification factor $s(\tilde{k},\tilde{r})$ is displayed on figure 7 for the maximal range of variation of the scaled coordinates $\tilde{r}$ and $\tilde{k}$ above, i.e. $0 < \tilde{r} < We$ and $0 < \tilde{k} < \alpha We$. As expected from the above discussion, $s(\tilde{k},\tilde{r})$ increases with $\tilde{r}$ for small $\tilde{r}$, and then saturates, because of the thinning of the sheet. The increase is fairly independent of $\tilde{k}$ for small $\tilde{r}$ and the maximal amplification of wavenumber $\tilde{k}$

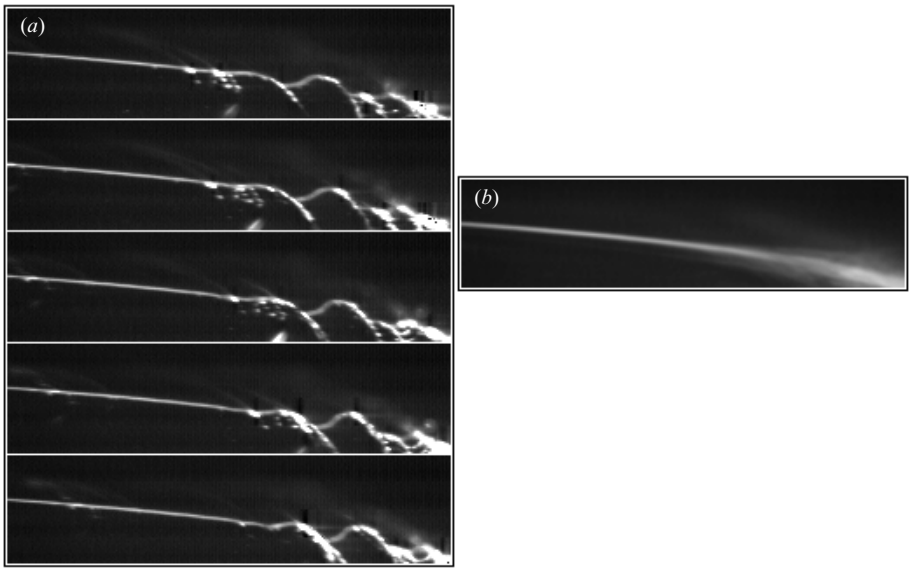

FIGURE 8. Transverse cut of the liquid sheet along its radius with a planar laser illumination. (*a*) A succession of instantaneous views showing the shape of the sheet as it breaks close to the rim, from top to bottom with a time interval of 2.2 ms. (*b*) Average probability of concentration field $c(r, y)$; r is the coordinate parallel to the sheet, and y is the coordinate perpendicular to it. The width of the images covers radial distances ranging from $r = 0$ to $50D_0$, with $D_0 = 3$ mm. Air/water, $We = 1600$.

is obtained for $s(\tilde{k}, We - \tilde{k}/\alpha)$, found from (15) to be close to

$$s(\tilde{k}, We - \tilde{k}/\alpha) \approx \frac{\alpha\pi We^2}{128} \left(\frac{\tilde{k}}{\alpha We}\right)^{1/2} \left(1 - \frac{\tilde{k}}{\alpha We}\right)^2, \tag{16}$$

and whose maximum provides the most amplified wavenumber

$$\tilde{k}_{\max} = \frac{\alpha We}{5}, \tag{17}$$

consistently with equation (6). The transient growth along the sheet radius of the disturbances can be followed by making a cut through the liquid, perpendicular to the undisturbed interface, using a planar laser illumination. When the liquid has been seeded with a fluorescent dye, the sheet appears as a bright corrugated ribbon on a dark background (figure 8). As long as the liquid sheet remains continuous, that is before it breaks into droplets, the evolution of the transverse width of the brightness concentration profile along r reflects directly the disturbance spatial amplification which can, at least in the linear part of the instability development, be compared with (15).

Specifically, if $c(r, y)$ denotes the brightness concentration of the average field of figure 8(*b*), the thickness $\delta(r) = c(r, 0)/(\mathrm{d}c(r, y)/\mathrm{d}y)_{\max}$ is a measure of the mean transverse width of the liquid sheet profile, reflecting the instability amplitude to some proportionality factor (see also Taylor 1960; Asare, Takahashi & Hoffman 1981). The evolution of $\delta(r)$ is shown on figure 9 for $We = 1600$. Also shown on figure 9 is the prediction from the amplification factor of equation (15) corresponding to the most

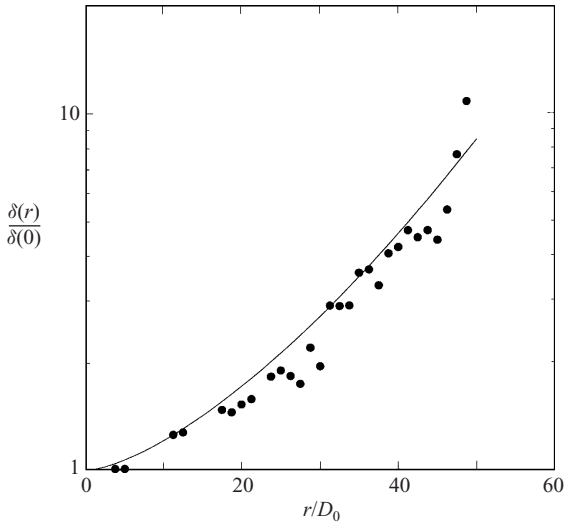

FIGURE 9. Radial evolution of the thickness $\delta(r)$ of the concentration profile $c(r, y)$ for $We = 1600$, $\alpha = 1.2 \times 10^{-3}$ (air/water). The continuous line is the amplification predicted by equation (18).

amplified wavenumber derived in (17)

$$s(\tilde{k}_{\max}, \tilde{r}) \approx \alpha We^{1/2} \tilde{r}^{3/2}. \tag{18}$$

The radial increase of $\delta(r)$ is stronger than exponential because of the thinning of the liquid sheet, as can be seen from equations (12) and (15).

4.3. *Group velocity*

Another specific consequence of the liquid sheet thinning due to its axisymmetric development is the radial evolution of the group velocity $v_g = \mathrm{d}\omega_r/\mathrm{d}k$:

$$v_g = U_0 \frac{2\alpha\tilde{r}/\tilde{k} + 1}{(\alpha\tilde{r}/\tilde{k} + 1)^2}. \tag{19}$$

The group velocity can be measured from the radial displacement of the crests of the sheet disturbances, on a time-resolved movie of the instability development, as illustrated on figure 10. It is observed, as shown on figure 11, that the velocity of the crests gradually decreases as they approach the sheet rim, where they almost stop as they break into droplets. The regular decrease of their group velocity far from the rim is compared on figure 11 with the one expected from equation (19) for, again, the most amplified wavenumber $k_{\max}$. Note that the same procedure of using a passive marker on the liquid had confirmed, as explained in Clanet & Villermaux 2002, that the liquid radial velocity is constant and equal to U_0 from the impact to the rim in the smooth regime.

Finally, and once the group velocity of the crests is known, the mode selection of this instability can be investigated experimentally by measuring the duration of the time interval between two crests as they reach the rim. This is an observable which is determined in a much more deterministic way than the direct visualization of the wavelength on instantaneous pictures. Indeed, the gradient of group velocity on r induces a slight wave compression close to the rim which makes the measurement of the wavelength fuzzy. On the other hand, this compression phenomenon does not

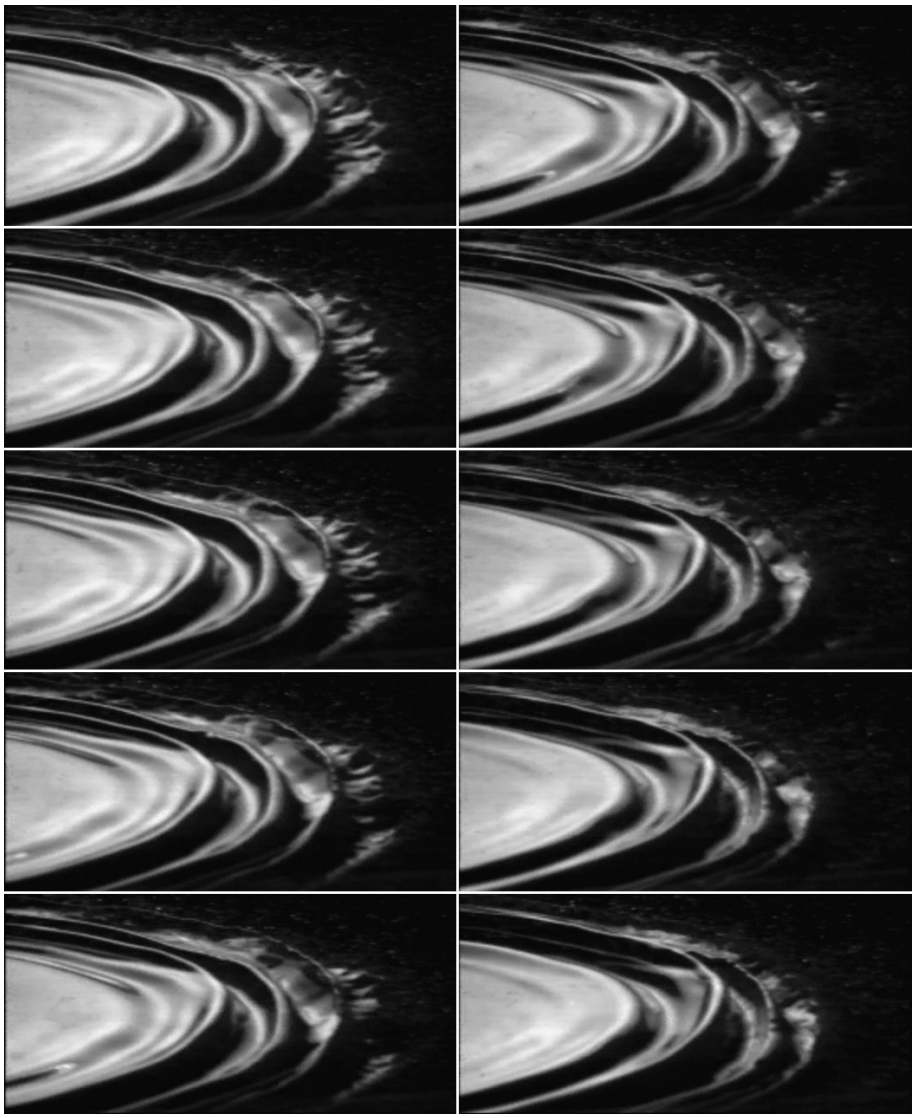

FIGURE 10. A time-resolved series of the sheet undulation waves propagating towards the rim. Ethanol/air ($\alpha = 1.2/800$). $We = 1800$. The images are equally spaced in time, from top to bottom, left then right, and the whole series last for about 8 ms. The distance between two consecutive crests is about 3 cm.

affect the passage frequency $1/\tau$ of the sheet undulation crests, which is conserved along r. From (17) and (19), we have, with $\lambda = 2\pi/k_{\max}$.

$$\tau = \frac{\lambda}{v_g} = \frac{10\pi\sigma}{\rho_a U_0^3}, \tag{20}$$

a relation which is found to be in quantitative agreement with the measurements of τ for a range of Weber number covering a decade (figure 12).

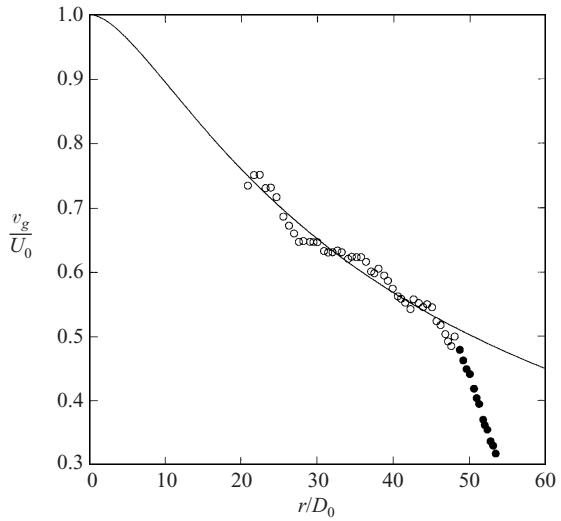

FIGURE 11. Radial evolution of the velocity of the crests as they approach the rim for conditions identical to those of figure 10. The rim location is $R/D_0 = 50$ approximately. The continuous line is the dependence expected from equation (19) with $\tilde{k} = \tilde{k}_{\max}$. Note the rapid decrease of the speed of the waves (highlighted by the black dots) as they reach the rim and break into droplets.

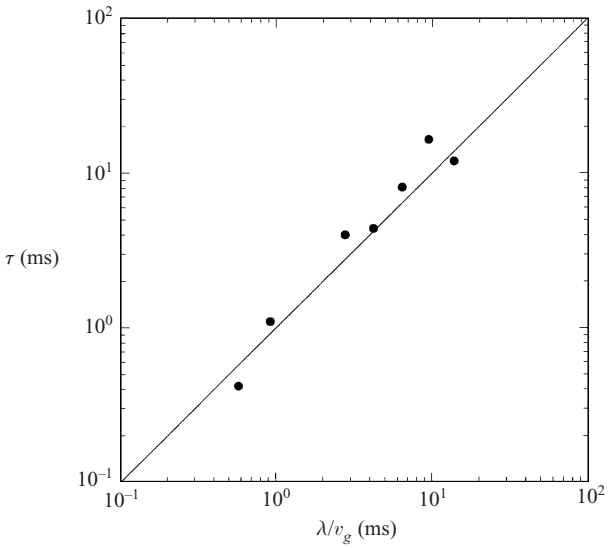

FIGURE 12. Time interval τ between the passage of two consecutive crests at the rim compared to the expected interval of equation (20). Ethanol/air ($\alpha = 1.2/800$). The Weber number ranges from 10^3 to about 10^4 for these measurements.

5. The sheet disintegration criterion

From the features of the primary shear instability, we propose in the following a possible mechanism for the sheet disintegration. The aim is to predict the critical amplitude of the primary waves on the sheet at breakup, the radial location of the breakup, and the resulting droplet sizes.

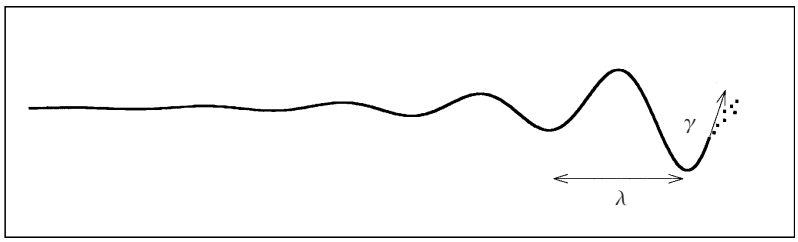

FIGURE 13. Sketch of the shape of the liquid sheet $y(r,t)$ close to the rim showing a primary undulation of wavelength λ and the component γ of the acceleration experienced by the liquid parallel to the sheet.

5.1. *Acceleration at the rim*

In the frame of reference of the liquid propagating at constant velocity in the plane of the sheet, the periodic passage of the sheet undulations gives the liquid a periodic acceleration. The forces acting on a fluid particle moving in the sheet are nearly balanced: they are strictly balanced when $\alpha = 0$ (when the surrounding medium has a vanishingly small density) since in that case the sheet sustains neutrally stable waves resulting from the equilibrium between the liquid inertia and surface tension as shown by equation (7). When $\alpha \neq 0$, the disequilibrium induced by the depressions in the ambient phase result in the increase of the wave amplitude through the instability we have described in § 3. However, because of the difference in velocity $U_0 - v_g$ between the liquid and the waves, a fluid particle experiences transient accelerations. In particular, the component γ of the acceleration parallel to the sheet is alternately directed towards the incoming liquid and in the opposite direction (figure 13). This component of the acceleration is obviously the one that tears off the drops from the continuous part of the sheet at its rim, when the force balance ensured by surface tension has been broken. Similarly, the rim destabilization of rotating liquid films, such as those formed in spinning cups (see e.g. Eisenklam 1964; Fraser *et al.* 1963; Hinze & Milborn 1950) involve centrifugal forces whose direction lies in the plane of the sheet. The problem to solve is to find how these transient accelerations are involved in the process which prevents the sheet from remaining continuous, i.e. the breakup process at the rim.

We know from Rayleigh (1883) and Taylor (1950), that a density interface separating two infinite media subjected to an acceleration may be unstable. The instability occurs under gravity when a heavy layer is supported by a light one (which was the situation investigated by Rayleigh) and equivalently under the acceleration of the whole system in the direction towards the denser fluid. A layer of dense fluid immersed in a lighter fluid accelerated perpendicular to its plane is also unstable, as shown by Taylor (see also Keller & Kolodoner 1954). For a density interface separating two infinite media subjected to an acceleration γ, as is the case if one considers the sheet rim and the component of the acceleration parallel to the sheet, the range of unstable wavenumbers extends from 0 to $k_c = \sqrt{(\rho - \rho_a)\gamma/\sigma}$ and the most amplified wavenumber is $k_c/\sqrt{3}$.

The procedure adopted here is the following: we assume the existence of a Rayleigh–Taylor type of instability at the sheet rim triggered by the periodic passage of the sheet undulations. We compute the magnitude of the acceleration γ induced by the undulations as a function of their wavelength λ, amplitude ξ and passage period τ. Then we compute the growth rate s of the Rayleigh–Taylor instability as a function

of γ and we assume that the instability will set in as soon as s^{-1} is shorter than the persistence time of γ. Since the acceleration γ is oscillating in time, we mean by 'persistence time' the time during which the acceleration is larger than a given level. From there, the problem is closed, providing the intensity of γ, the corresponding critical amplitude ξ and finally the typical size of the small-scale rim indentations, namely the Rayleigh–Taylor wavelength $\lambda_\perp \sim \sqrt{\sigma/\rho\gamma}$.

Since the amplitude of the primary wave is a function of the radial location, the determination of the critical amplitude for breakup also sets the sheet radius R. The droplet size resulting from the pieces of liquid torn off from the sheet rim follows. The primary wavelength is always smaller than the sheet radius (i.e. $\lambda/R \ll 1$) and we formalize the problem in a Cartesian frame, the direction r being aligned with the radius of the sheet. The shape of the undulated sheet close to the rim is

$$y(r,t) = \xi(R)\cos\left(2\pi\left(\frac{t}{\tau} - \frac{r}{\lambda}\right)\right), \tag{21}$$

where $\xi(R)$ is the amplitude of the crest corrugations close to the rim, τ the passage period of the crests at the rim given by equation (20), and λ their wavelength. The acceleration γ experienced by the sheet parallel to itself is $\gamma = (\partial^2 y/\partial t^2)(\partial y/\partial r)$, that is

$$\gamma \sim \frac{\lambda}{\tau^2}\left(\frac{\xi(R)}{\lambda}\right)^2 \sin\left(4\pi\frac{t}{\tau}\right) = \frac{U_0^2}{\lambda}\left(\frac{\xi(R)}{\lambda}\right)^2 \sin\left(4\pi\frac{t}{\tau}\right) \tag{22}$$

at the rim. We have deliberately removed the spatial constant ($r = R$) phase factor in (22), since the discussion below will only be concerned with the temporal modulation of γ. We have for simplicity approximated the velocity difference between a fluid particle in the sheet and the waves velocity by U_0, a fair estimate close to the rim. The oscillation frequency of γ is twice the passage frequency. Note that γ is, as expected, a function of the aspect ratio of the wave $\xi(R)/\lambda$. During half of the oscillation period of γ, that is for a maximal time interval $\lambda/4U_0$, the acceleration γ is negative, oriented in the direction towards the liquid. During that time interval, the rim is thus potentially unstable in the sense of Rayleigh–Taylor. For the instability to occur, however, the persistence time of a given acceleration level γ has to be larger than the inverse of the growth rate of the Rayleigh–Taylor instability based on this acceleration level. Specifically, the (inviscid) instability growth rate is

$$s \sim \left(\frac{\rho\gamma^3}{\sigma}\right)^{1/4}, \tag{23}$$

and if $\Delta t(G)$ represents the time interval during which the acceleration is larger than, say $G\gamma_{\max}$ (see figure 14*a*), with $\gamma_{\max} = (U_0^2/\lambda)(\xi(R)/\lambda)^2$, then the condition for onset of the instability is

$$\Delta t(G) > s^{-1}(G). \tag{24}$$

The time interval $\Delta t(G)$ is

$$\Delta t(G) = \frac{\lambda}{4U_0}\left(1 - \frac{2}{\pi}\sin^{-1}(G)\right), \tag{25}$$

and together with relations (17) and (23), condition (24) provides

$$G^3\left(1 - \frac{2}{\pi}\sin^{-1}(G)\right)^4\left(\frac{\xi(R)}{\lambda}\right)^6 > \alpha. \tag{26}$$

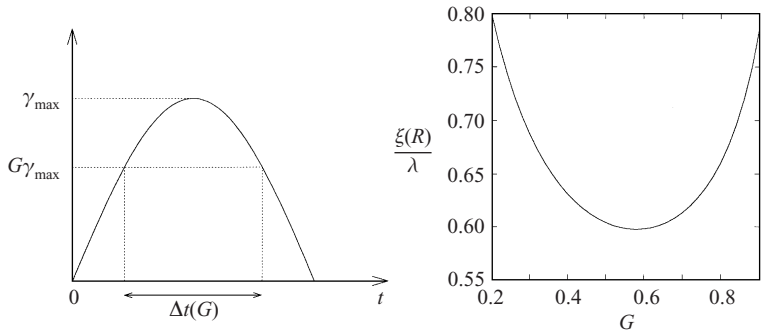

FIGURE 14. (*a*) Half of the oscillation period of the sheet acceleration during which the rim is Rayleigh–Taylor unstable. $\Delta t(G)$ represents the time interval during which the acceleration is larger than $G\gamma_{max}$. (*b*) The aspect ratio of the undulation waves at the rim as they break, $\xi(R)/\lambda$, versus G given by equation (26).

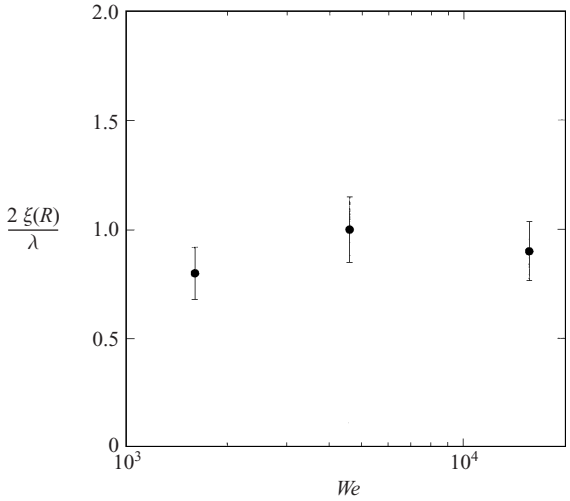

FIGURE 15. The aspect ratio of the undulation waves at the rim as they break, $2\xi(R)/\lambda$, as a function of the Weber number.

It is seen on figure 14(*b*) that the above condition is fulfilled, for $\alpha = 1.2/1000$, once

$$\frac{\xi(R)}{\lambda} > 0.6 = 1.85 \times \alpha^{1/6} \quad \text{and} \quad G \approx 0.58. \tag{27}$$

Note that since $G < 1$ by construction, condition (26) can be approached analytically: making $\sin^{-1}(G) \approx G$, one finds that $\xi(R)/\lambda > (14^7\alpha/8^4(3\pi)^3)^{1/6} \approx 0.6$ for $G = 3\pi/14$, consistently with the full solution of (26) displayed on figure 14(*b*). For a broad range of Weber numbers in the flag instability regime, the aspect ratio of the waves is found to be a constant, to the extent that this quantity can be measured with accuracy (see figure 15), and of order unity, consistently with (27). In the scenario we have depicted above, the order of magnitude of the small-scale rim indentations is expected to be given by the Rayleigh–Taylor wavelength $\lambda_\perp \sim \sqrt{\sigma/\rho\gamma}$ estimated at the critical acceleration corresponding to the conditions (27), and is therefore

$$\lambda_\perp \sim \frac{\sigma}{\rho_a U_0^2}\left(\frac{\rho_a}{\rho}\right)^{1/3}, \quad \text{i.e.} \quad \frac{\lambda_\perp}{\lambda} \approx \alpha^{1/3} \approx 0.1, \tag{28}$$

an acceptable order of magnitude if one considers, for instance, figure 2. Note that this scenario is not intended to account for the waviness of liquid sheets at a scale much larger than their thickness, as one can see from figure 2, whose origin requires examination (see e.g. Bernal & Roshko 1986; Kim & Sirignano 2000), but rather is intended to represent the fine-scale indentations of rim as droplets tear off. The mechanism we have proposed is, in essence, distinct from a parametric instability, or Faraday mechanism. The reason is that the basic state, that is the shape of the rim in the smooth regime, does not sustain waves (the large cusps at the sheet rim are steady on a short timescale, see Clanet & Villermaux 2002), which could otherwise be excited by the incoming undulations of the sheet. On the contrary, the rim behaves, in the scenario we describe, as a filter, whose motion follows those imposed by the incoming undulations up to a cut-off frequency, equal to the growth rate of a Rayleigh–Taylor instability, above which it disintegrates.

5.2. *Liquid sheet radius*

We have just shown that the liquid sheet is likely to break up once the primary undulations have reached a critical aspect ratio, namely $\xi(R)/\lambda \approx 1.85 \times \alpha^{1/6}$. This, since we know how the amplitude depends on the radial location (equation (18) and figure 9), conversely fixes the sheet radius R. Since

$$\ln\left(\frac{\xi(r)}{\xi(0)}\right) \approx \alpha We^{1/2} r^{3/2}, \tag{29}$$

the critical radius is

$$(\alpha^{1/2} We)^{1/3} \frac{\alpha^{1/2} R}{D_0} \sim \left(\ln\left(\frac{1.85 D_0/\xi_0}{\alpha^{5/6} We}\right)\right)^{2/3} \approx \text{const}, \tag{30}$$

the logarithm evolving only slightly with the Weber number because of the large value of its argument due to the large value of $D_0/\xi(0)$.

The sheet radius R/D_0 decreases like $\alpha^{-2/3} We^{-1/3}$ with increasing Weber number, because the critical aspect ratio of the primary waves is reached earlier when the Weber number is larger. The above evolution law for the sheet radius is expected to hold once R given by (30) becomes smaller than the radius characterizing the smooth regime and which was found to be $R/D_0 \sim We$ (see Clanet & Villermaux 2002). Therefore, the critical Weber number above which the flag instability regime sets in is such that

$$\alpha^{1/2} We_c = \text{const}. \tag{31}$$

The value of the constant is 40, as can be seen from figure 16.

Equation (31) has a special meaning as it expresses the crossover between the two acceleration scales which cause the droplets to detach from the continuous liquid sheet. The relevant acceleration in the smooth regime was shown in Clanet & Villermaux (2002) to be given by U_0^2/R, where R is the radius of curvature of the cusps-like indentations close to the sheet rim, given by the sheet radius $R/D_0 \sim \rho U_0^2 D_0/\sigma$. We have shown here that the corresponding acceleration is U_0^2/λ, with $\lambda \sim \sigma/\rho_a U_0^2$. Equation (31) expresses the condition $U_0^2/\lambda > U_0^2/R$, within numerical prefactors. Note that equation (31) also means that the liquid sheets at the onset of the flag regime have self-similar shapes, whatever the initial diameter D_0, since λ/R is a constant at onset. The acceleration due to gravity g is always negligible in the flapping regime. The ratio $U_0^2/g\lambda = \alpha We(U_0^2/gD_0)$ is much larger than unity since $\alpha We = O(1)$ and the Froude number $Fr = U_0^2/gD_0 \gg 1$.

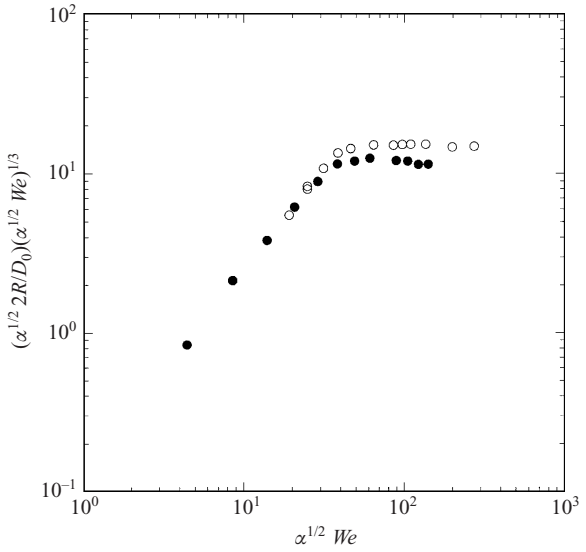

FIGURE 16. Sheet radius dependence on the Weber number and density ratio in the scaled coordinates of equation (30): •, air ($\rho_a = 1.2\,\mathrm{kg\,m^{-3}}$); ○, SF_6 ($\rho_a = 6\,\mathrm{kg\,m^{-3}}$).

Figure 16 shows the variation of the radius R for two distinct experiments, using the same injector and the same liquid (i.e. with the same D_0 and therefore the same We for a given exit velocity U_0), but with a different density for the ambient gas, therefore allowing to examine the intrinsic influence of the density ratio α. We have $\alpha = 1.2/1000$ for the couple air/water, and $\alpha = 1.2 \times 5/1000$ for the couple SF_6/water. It is seen on figure 16 (the data are those of figure 3) that the evolution of the sheet radius for the two experiments collapse when plotted against the scaled Weber number $\alpha^{1/2}We$ for the two different values of the parameter α.

5.3. *Droplet size*

Drops in this regime are released in a 'chaplet' at the tip of the Rayleigh–Taylor indentations. Those have the shape of strips of liquid which, once they are formed, further fragment into disjointed droplets by a Plateau capillary instability, and whose size is therefore very close to the instability wavelength $\lambda_\perp$. Other examples in related contexts can be found in the case of unstable liquid surfaces accelerated at a constant level perpendicular to their plane (Lewis 1950), or concerning the drops formed from sheets centrifuged in spinning cups (Eisenklam 1964). It is thus expected that the drop size d will scale like

$$d \sim \lambda_\perp \sim \frac{D_0}{\alpha^{2/3}We}. \tag{32}$$

As shown on figure 17, the measured droplet sizes are not inconsistent with this trend. In particular, a good collapse is obtained between water and ethanol, for two different values of α. The ratio $\lambda_\perp/h(R) \sim (\alpha We)^{-4/3}$ eventually becomes smaller than unity as We increases so that the droplet size becomes smaller than the thickness of the sheet $h(R)$ at its rim.

Note that equation (32) can also be interpreted as a force balance involving the acceleration seen by the droplets as they detach, in the spirit of the derivation in Clanet & Villermaux (2002). At the very moment when a droplet of size d detaches

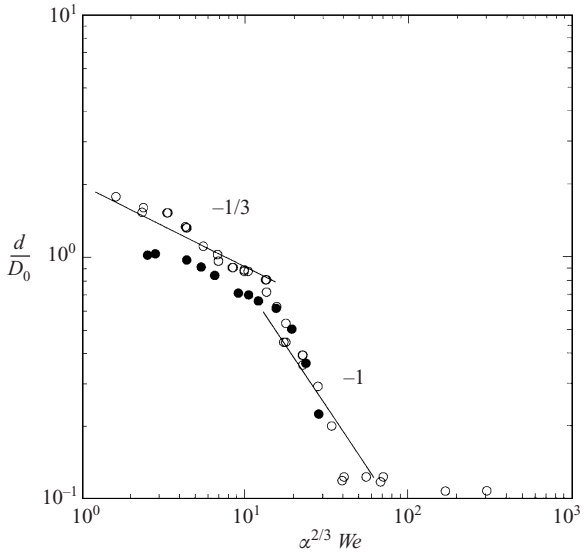

FIGURE 17. Droplet mean arithmetic diameter d/D_0 versus Weber number scaled by the density ratio α (see equations (30) and (31)). •, $D_0 = 2.7$ mm, water ($\alpha = 1.2/1000$); ○, $D_0 = 2.7$ mm, ethanol ($\alpha = 1.2/800$). The flag instability regime corresponds to $\alpha^{1/2}We > 40$, that is $\alpha^{2/3}We \gtrsim 13$ since $\alpha = O(10^{-3})$. The lines are drawn to guide the eyes.

from a strip of thickness $\lambda_\perp$ under the action of an acceleration γ we have

$$\rho d^3\gamma \sim \sigma\lambda_\perp, \tag{33}$$

a relation which, with γ given by condition (27) and $\lambda_\perp$ given by (28) leads identically to (32), not surprisingly since the two descriptions have the same ingredients.

6. Conclusion and discussion

The objective of this study was to elucidate the mechanisms of drop formation from a liquid sheet, a generic object which is frequently formed, at least transitorily, in various atomization processes. We have followed the development of the sheet from the impact point of the jet which gives birth to it, up to its disappearence into a set of discrete droplets. The study has been substantiated experimentally for a broad range of control parameters, using different liquids and ambient medium densities.

For a drop to detach from the continuous part of a liquid volume, the body force acting on it has to overcome surface tension effects. This simple fact has led us to investigate in Clanet & Villermaux (2002) the intensity of the centrifugal force experienced by the detaching drops at the rim of the cusp-like indentations of a smooth, radially expanding liquid sheet resulting from the impact of a jet on a solid, circular surface. The present paper is devoted to the regime where the sheet interacts with the surrounding medium. This interaction amounts to a shear instability which induces a flag-like, sinuous unstable motion of the liquid which destabilizes, and detaches from the continuous portion of the sheet because of the acceleration associated with the passage of the crests of instability at the sheet rim. The critical amplitude of the wave crests for which the atomization of the sheet occurs is linked to the instability properties of the sheet, which also determines the droplet size d torn

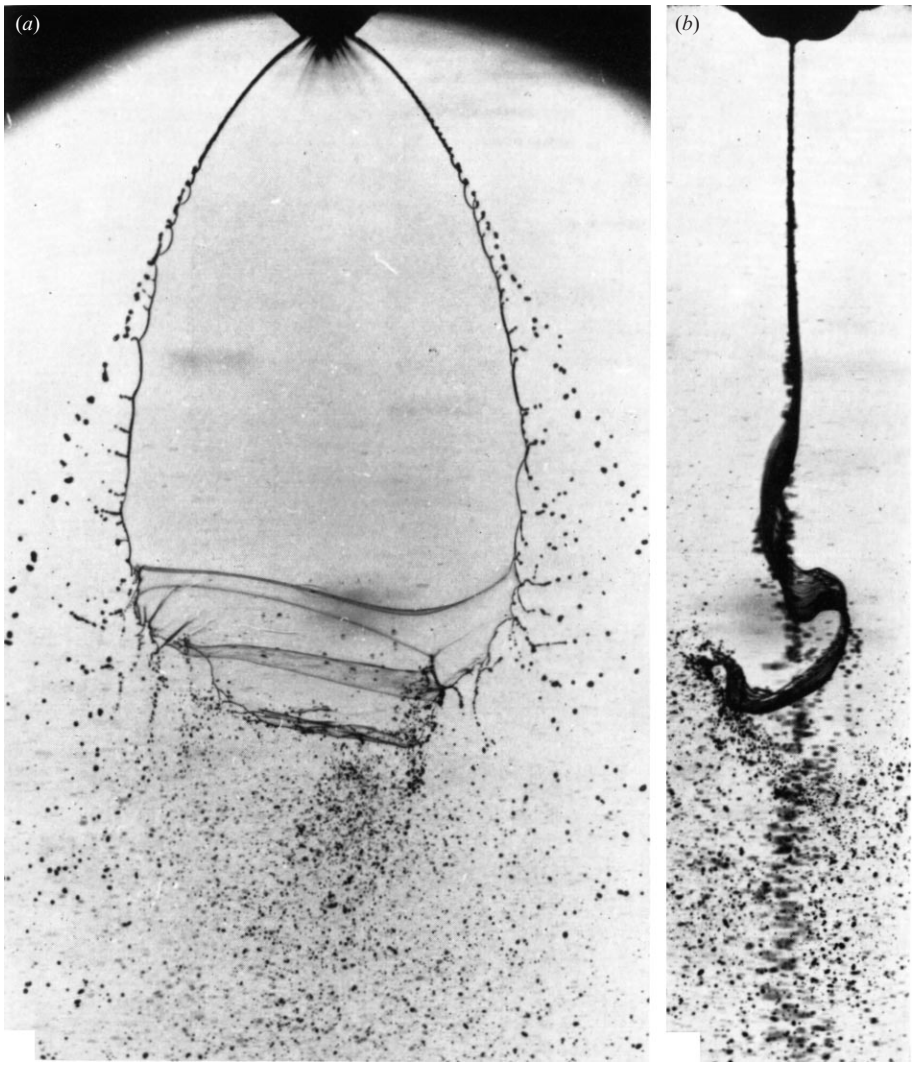

FIGURE 18. Liquid sheet issuing from a fan spray nozzle ((*a*) front and (*b*) side views, reproduced from Crapper *et al.* 1973) showing both the formation of drops at the edge of the curved rim of the sheet by a centrifugal instability, and the formation of finer droplets at the bottom of the sheet due to the flag instability.

off from the continuous part of the liquid and the sheet radius R as

$$d/D_0 \sim \alpha^{-2/3} We^{-1} \quad \text{and} \quad R/D_0 \sim \alpha^{-2/3} We^{-1/3},$$

where D_0 is the initial jet diameter and $We = \rho U_0^2 D_0/\sigma$ is the impact Weber number. These laws are valid for $\alpha^{1/2} We > 40$. This condition expresses the crossover between the two acceleration scales causing the droplets to detach from the continuous liquid sheet. In the smooth regime, the relevant acceleration is given by U_0^2/R, where R is the radius of curvature of the cusp-like indentations close to the sheet rim, given by the sheet radius $R/D_0 \sim \rho U_0^2 D_0/\sigma$. In the flag regime, the corresponding acceleration is U_0^2/λ, with $\lambda \sim \sigma/\rho_a U_0^2$, and the transition condition corresponds to $U_0^2/\lambda > U_0^2/R$.

The above breakup scenario is in contrast with the one imagined by Fraser *et al.*

(1962), in discussing the size of drops formed by a sheet issuing from a fan spray nozzle. These authors imagined that a strip of liquid of width λ and thickness h detaches from the sheet, forming a cylindrical ligament from which, by a Rayleigh capillary instability, drops are formed whose size was expected to scale as $\sqrt{\lambda h} \sim We^{-1/3}$, since $\lambda \sim We^{-1}$ and $h \sim We^{1/3}$ in this regime. Their measurements display a dependence of the droplet size close to $We^{-1/3}$. However, this scenario violates the Plateau–Rayleigh theorem, stating that a flat liquid sheet is linearly stable with respect to surface tension effects, as opposed to the circular jet geometry, and neither on their photographs, nor on ours in the related system we have studied, does a strip of liquid detach from the sheet. On the contrary, the sheet produced from the fan nozzle in Fraser *et al.*'s experiment (see also Crapper *et al.* 1973; Dorman 1952 and figure 18), takes the shape of a leaf with curved rims and presents, at its edges, a series of cusps very similar to those we observe in the smooth regime and from which big (compared to the local sheet thickness) droplets detach. It is plausible that the measurements of Fraser *et al.* are in fact reminiscent of the process we analysed in Clanet & Villermaux (2002) where the droplet size was shown to decay like $We^{-1/3}$.

The scenario we have depicted here, as well as providing satisfactory scaling relations for the present study, may have a relevance in the more general context of 'airblast atomization' (Lefebvre 1989), that is high-speed gas-assisted drop formation. In these processes, a shear instability is usually responsible for the primary destabilization of the liquid phase, producing sheets, or ligaments which further degenerate into droplets. The Rayleigh–Taylor instability of the liquid interface induced by the acceleration caused by the shear instability is probably a relevant mechanism to consider in investigating the process of drop formation in these situations.

The work presented in this paper has been supported by the Société Européenne de Propulsion (SEP) under contract 910023. We thank Geoff Searby for helpful remarks, suggestions, and interest.

REFERENCES

Asare, H. R., Takahashi, R. K. & Hoffman, M. A. 1981 Liquid sheet jet experiments: comparison with linear theory. *Trans. ASME*: *J. Fluids Engng* **103**, 595–604.

Bayvel, L. & Orzechowski, Z. 1993 *Liquid Atomization.* Taylor & Francis.

Bernal, L. P. & Roshko, A. 1986 Streamwise vortex structure in plane mixing layers. *J. Fluid Mech.* **170**, 449–525.

Bourrières, F. J. 1939 Sur un phénomène d'oscillation auto-entretenue en mécanique des fluides réels. *Publications Scientifiques et Techniques du Ministère de l'Air* 147.

Clanet, C. & Villermaux, E. 2002 Life of a smooth liquid sheet. *J. Fluid Mech.* **462**, 307–340.

Crapper, G. D., Dombrowski, N., Jepson, W. P. & Pyott, G. 1973 A note on the growth of Kelvin–Helmholtz waves on thin liquid sheets. *J. Fluid Mech.* **57**, 671–672.

De Langre, E. & Ouvrard, A. E. 1999 Absolute and convective bending instabilities in fluid-conveying pipes. *J. Fluids Struct.* **13**, 663–680.

Dorman, R. G. 1952 The atomization of liquid in a flat spray. *Brit. J. Appl. Phys.* **3**, 189–192.

Eisenklam, P. 1964 On ligament formation from spinning discs and cups. *Chem. Engng Sci.* **19**, 693–694.

Fraser, R. P., Dombrowski, N. & Routley, J. H. 1963 The filming of liquids by spinning cups. *Chem. Engng Sci.* **18**, 323–337.

Fraser, R. P., Eisenklam, P., Dombrowski, N. & Hanson, D. 1962 Drop formation from rapidly moving liquid sheets. *AIChE J.* **8**, 672–680.

Hagerty, W. W. & Shea, J. F. 1955 A study of the stability of plane fluid sheets. *Trans. ASME*: *J. Appl. Mech.* **22**, 509–514.

Hinze, J. O. & Milborn, H. 1950 Atomization of liquid by means of a rotating cup. *Trans. ASME*: *J. Appl. Mech.* **17**, 145–153.

Huang, J. C. P. 1970 The break-up of axisymmetric liquid sheets. *J. Fluid Mech.* **43**, 305–319.

Keller, J. B. & Kolodoner, I. 1954 Instability of liquid surfaces and the formation of drops. *J. Appl. Phys.* **25**, 918–921.

Kim, I. & Sirignano, W. A. 2000 Three dimensional wave distortion and disintegration of thin planar liquid sheets. *J. Fluid Mech.* **410**, 147–183.

Lamb, H. 1932 *Hydrodynamics*. Cambridge University Press.

Lefebvre, A. H. 1989 *Atomization and Sprays*. Hemisphere.

Lewis, D. J. 1950 The instability of liquid surfaces when accelerated in a direction perpendicular to their planes. II. *Proc. R. Soc. Lond.* A **202**, 81–96.

Marmottant, P., Villermaux, E. & Clanet, C. 2000 Dynamic surface tension in an expanding circular liquid sheet. *J. Colloid Interface Sci.* **230**, 29–40.

Païdoussis, A. & Li, G. X. 1993 Pipes conveying fluid: a model dynamical problem. *J. Fluids Struct.* **7**, 137–204.

Rayleigh, Lord 1879 On the instability of jets. *Proc. R. Soc. Lond.* **X**, 4–13.

Rayleigh, Lord 1883 Investigation of the character of the equilibrium of an incompressible heavy fluid of variable density. *Proc. R. Soc. Lond.* **XIV**, 170–177.

Rayleigh, Lord 1891 Some applications of photography. *Nature* **XLIV**, 249–254.

Savart, F. 1833 Mémoire sur le choc d'une veine liquide lancée contre un plan circulaire. *Annales de Chimie* **54**, 56–87.

Squire, H. B. 1953 Investigation of the stability of a moving liquid film. *Brit. J. Appl. Phys.* **4**, 167–169.

Taylor, G. I. 1950 The instability of liquid surfaces when accelerated in a direction perpendicular to their planes. I. *Proc. R. Soc. Lond.* A **202**, 192–196.

Taylor, G. I. 1959*a* The dynamics of thin sheets of fluid. II Waves on fluid sheets. *Proc. R. Soc. Lond.* A **253**, 296–312.

Taylor, G. I. 1959*b* The dynamics of thin sheets of fluid. III Disintegration of fluid sheets. *Proc. R. Soc. Lond.* A **253**, 313–321.

Taylor, G. I. 1960 Formation of thin flat sheets of water. *Proc. R. Soc. Lond.* A **254**, 1–17.

Villermaux, E. 1998 Mixing and spray formation in coaxial jets. *J. Prop. Power* **14**, 807–817.

Weihs, D. 1978 Stability of thin, radially moving liquid sheets. *J. Fluid Mech.* **87**, 289–298.

York, J. L., Stubbs, H. E. & Tek, M. R. 1953 The mechanism of disintegration of liquid sheets. *Trans. ASME* 1279–1286.